

Temperature-induced phase transitions in the correlated quantum Hall state of bilayer graphene

M. Tanaka ^{1,*}, K. Watanabe ², T. Taniguchi ³, K. Nomura ⁴, S. Tarucha ⁵, and M. Yamamoto ^{5,†}

¹*Department of Applied Physics, University of Tokyo, Bunkyo-ku, Japan*

²*Research Center for Functional Materials, National Institute for Materials Science, Tsukuba-shi, Japan*

³*International Center for Material Nanoarchitectonics, National Institute for Material Science, Tsukuba-shi, Japan*

⁴*Department of Physics, Tohoku University, Sendai-shi, Japan*

⁵*Center for Emergent Matter Science, RIKEN, Wako-shi, Japan*

 (Received 27 August 2021; revised 28 January 2022; accepted 1 February 2022; published 24 February 2022)

The quantum Hall system can be used to study many-body physics owing to its multiple internal electronic degrees of freedom and tunability. While quantum phase transitions have been studied intensively, research on the temperature-induced phase transitions of this system is limited. We measured the pure bulk conductivity of a quantum Hall antiferromagnetic state in bilayer graphene over a wide range of temperatures and revealed the two-step phase transition associated with the breaking of the long-range order, i.e., the Kosterlitz-Thouless transition, and short-range antiferromagnetic order. Our findings are fundamental to understanding electron correlation in quantum Hall systems.

DOI: [10.1103/PhysRevB.105.075427](https://doi.org/10.1103/PhysRevB.105.075427)

I. INTRODUCTION

The quantum Hall state is one of the most strongly electronically correlated states owing to its quenched kinetic energy. When multiple internal electronic degrees of freedom exist, an exchange interaction stabilizes a many-body-ordered ground state if a one-particle Landau level (LL) is partially filled [1–3].

A well-known example that has been intensively studied is the double-layer quantum Hall system at the total filling factor $\nu = 1$ [3]. This system is considered as an easy-plane ferromagnet of the pseudospin defined by the layer degree of freedom. Rich varieties of phase transitions have been investigated for control parameters such as temperature, layer separation, magnetic field, interlayer charge imbalance, and interlayer tunneling. Observation and characterization of the yet elusive temperature-induced Kosterlitz-Thouless (KT) transition remains as one of the central and longstanding issues in this field.

As many-body-ordered states in quantum Hall systems are characterized by energy gap opening and ordering, they should have analogies with other correlated insulators such as Mott insulators and two-dimensional moiré flat band systems. Because both the interaction energy and one-particle energy of the quantum Hall state can be controlled by parameters such as the carrier density (filling factor), out-of-plane and in-plane magnetic field, and out-of-plane electric field, it can be a tunable experimental platform for investigating general correlated effects and phase transitions.

Although the quantum phase transitions in quantum Hall states have been extensively studied both experimentally and theoretically, few studies have been conducted on

temperature-induced classical phase transitions [4–6]. This is because, theoretically, finite temperature behavior is much more difficult to investigate than zero-temperature behavior. Furthermore, experimentally, the coexistence of the bulk and edge states makes the temperature dependence of observables more complex than in homogeneous systems.

The zero-energy LL of bilayer graphene (BLG) is a promising platform for studying temperature-induced phase transitions. It exhibits various ordered states owing to the interplay of spin, layer, and orbital degrees of freedom, and controllability of the layer degree of freedom by an out-of-plane external electric field (displacement field D) [7–37]. At $\nu = 0$ (half filling of the zero-energy LL), the canted antiferromagnetic (CAF) state is thought to be stabilized by the short-range Coulomb interaction under a small D , whereas the layer polarized (LP) state is favored under a large D [7–28]. The ferromagnetic state is favored for enhanced Zeeman energy by a tilted magnetic field [15–18, 25–27]. In this paper, we focus on the CAF state, where the spins tend to align ferromagnetically within each layer and antiferromagnetically between the layers [25–27] [Fig. 1(a)]. The spins tend to lie in the plane with a small canting along the out-of-plane magnetic field to minimize both the antiferromagnetic exchange energy and Zeeman energy. Under a perpendicular magnetic field, the degree of canting is estimated to be only $1\text{--}2^\circ$ [25]; therefore, we can treat the CAF state as an ideal easy-plane antiferromagnet with $U(1)$ symmetry. It is also thought to be stabilized in the $\nu = 0$ state of monolayer graphene without staggered potential, where the layer degree of freedom in BLG is replaced with the sublattice degree of freedom.

Importantly, the CAF state does not have a zero-gap edge state unless the edge is a zigzag edge, owing to valley scattering at the edge. This simplifies the analysis of the temperature dependence of its bulk conductivity. In addition, the energy gap of the CAF state in BLG is much larger than that in a double-layer semiconductor quantum well [2], owing to the

*Corresponding author: miuko.t@gmail.com

†Corresponding author: michihisa.yamamoto@riken.jp

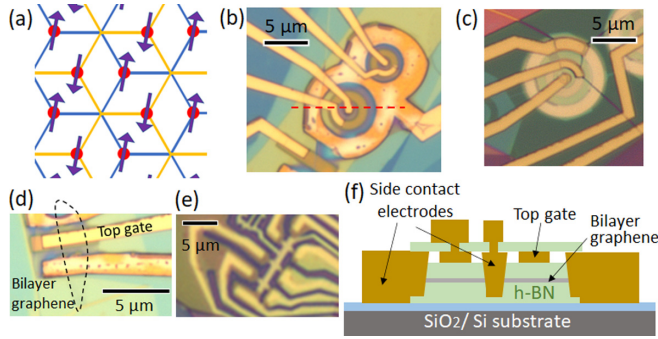


FIG. 1. Schematic of the canted antiferromagnetic (CAF) state and sample structure. (a) Configuration of the spins in the CAF state in bilayer graphene (BLG). The orange (blue) lines are the top (bottom) layers of the BLG. The red dots indicate the electrons, and their spins are indicated by the purple arrows. Optical microscope image of (b) Corbino 1, (c) Corbino 2, (d) two-terminal, and (e) Hall bar samples. (f) Schematic cross-section along the broken red line in (b). BLG is encapsulated by high-quality hexagonal boron nitride (h-BN) crystals with a thickness of 30–50 nm and sandwiched between the gold top gate and *p*-doped Si back gate.

smaller separation between layers, which increases the phase transition temperature.

The CAF state has also attracted considerable interest for its unique electronic transport properties. Long-range spin current transport arising from the easy-plane antiferromagnetic order [38–41], a kind of charge-neutral current originating from the spin-dependent layer polarization [42,43], and KT-like critical behavior of the conductance [11,44] have been observed. In addition, recent theories indicate the easy-plane antiferromagnetism in magic-angle-twisted BLG, which is like the CAF, as an origin of its superconductivity [45].

Previously, the temperature dependence of the conductivity of the CAF state was measured in limited temperature ranges [11,15,18]. However, few discussions have been made on temperature-induced phase transitions, as will be discussed later.

In this paper, we employed Corbino samples, which eliminate any type of edge transport to certainly measure the bulk conductivity in the CAF state and to study its temperature-induced phase transition. The observed non-monotonic temperature dependence of the bulk conductivity implies a two-step phase transition, which is explained well by the two energy scales of the CAF state: the short- and long-range Coulomb interaction energies.

II. SAMPLES AND METHODS

Our measurements employed four samples: Corbino 1, Corbino 2, two-terminal, and a Hall bar. All the samples were dual-gated BLG encapsulated by hexagonal boron nitride (h-BN) [Figs. 1(b)–1(f)] and fabricated by the dry transfer technique (details are provided in Appendix A). For Corbino 1 and 2, the dimensions of the active region covered with the top gate are the same [Figs. 1(b) and 1(c)]. While a *p*-doped Si substrate is used as a back gate for Corbino 1, a graphite back

gate which was patterned in the same shape as the top gate is used for Corbino 2. For Corbino 2, the nonactive region, which is not covered with the top gate, is heavily doped by the Si back gate. Therefore, most of the measured resistance originates from the active region. For Corbino 1, the resistance is the series resistance of the active and nonactive regions. Because the CAF state is established at $V_{TG} = 0$ in Corbino 1, the active and nonactive regions homogeneously become the CAF state under these conditions. This ensures the validity of the temperature-dependence measurement, as mentioned later.

Although the CAF state generally has no ballistic edge state owing to valley scattering at the edge [7–16,25–28], there is a possibility of diffusive edge transport owing to the hopping transport across sparsely existing zigzag edge regions [46]. The Corbino samples, which do not experience edge transport, allow for the measurement of pure bulk conductivity.

The conductivity was measured by a four-probe technique using lock-in amplifiers (3.77 Hz) with a constant current of ~ 3 nA.

III. RESULTS AND DISCUSSIONS

A. Gate dependence

In Fig. 2, we show the carrier density n and displacement field D dependence of the conductivity of Corbino 1 and 2, which was obtained from its gate voltage dependence under a perpendicular magnetic field $B = 0$ and 9 T at temperature $T = 2.3$ K. Here, n and D are determined by $n = \frac{\epsilon_{TG}}{ed_{TG}} V_{TG} + \frac{\epsilon_{BG}}{ed_{BG}} V_{BG}$ and $D = -\frac{\epsilon_{TG}}{d_{TG}} V_{TG} + \frac{\epsilon_{BG}}{d_{BG}} V_{BG}$, where ϵ_{TG} and ϵ_{BG} are dielectric constants of the insulating layers for the top and back gates, e is the elementary charge, and d_{TG} and d_{BG} are thicknesses of the insulating layers for the top and back gates determined by atomic force microscopy (AFM) measurement, respectively. We adopted $\epsilon_{h-BN} \cong 4\epsilon_0$ and $\epsilon_{SiO_2} \cong 3.58\epsilon_0$ (detail of the conversion is provided in Appendix B). Periodic conductivity dips due to the formation of LLs were observed under a magnetic field and assigned to filling factors of $\pm 8, \pm 4, \pm 3, \pm 2, \pm 1$, and 0, as indicated in Figs. 2(c) and 2(d). In Corbino 1, diagonal lines appeared in a direction perpendicular to the V_{BG} axis [blue arrows in Figs. 2(a) and 2(c)]. These lines corresponded to the minimum conductivity of the inactive region not covered by the top gate. On the other hand, the inactive region in Corbino 2 was highly doped by the Si back gate, and its conductivity was much higher than that of the active region. Therefore, the measured conductivity was mainly determined by the active region, and the diagonal lines were not observed. Focusing on $\nu = 0$ ($n = 0$), we found that the conductance dip vanished around $|D| = 0.16$ V/nm in Corbino 2. The two (separated) insulating states that appeared at $|D| < 0.16$ V/nm and $|D| > 0.16$ V/nm were assigned to the CAF and LP states, respectively [15,25–28].

The phase transition from the CAF state to the LP state was more clearly observed in the D and B dependences at $n = 0$ [Fig. 2(e)]. The displacement field D^* at the boundary between the CAF and LP regions linearly increases as B increases, which is quantitatively consistent with the results of

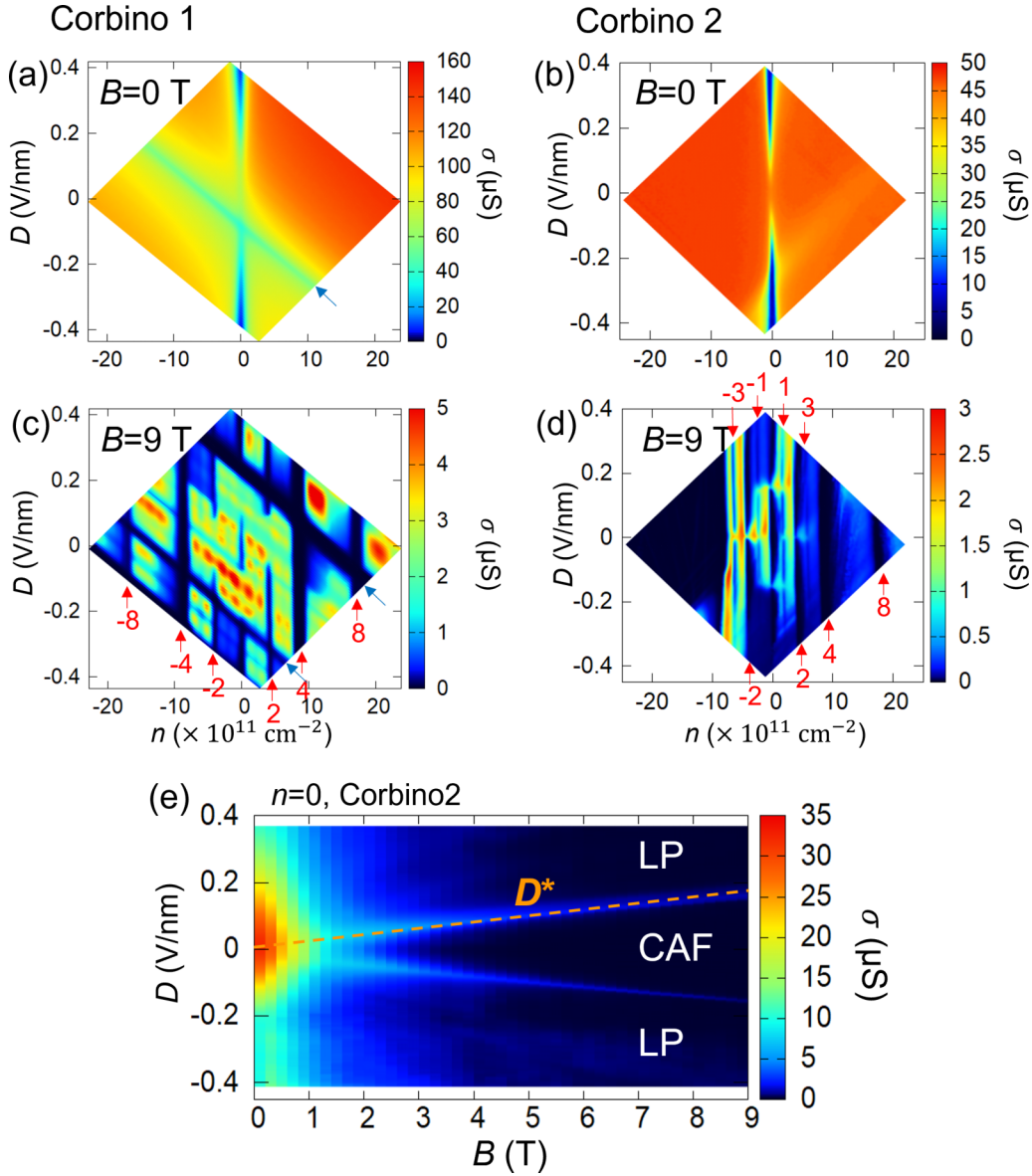


FIG. 2. n (carrier density) and D (displacement field) dependence of the conductivity in Corbino samples. A plot of conductivity σ vs the carrier density n and displacement field D at $T = 2.3$ K for (a) Corbino 1 at $B = 0$ T, (b) Corbino 2 at $B = 0$ T, (c) Corbino 1 at $B = 9$ T, and (d) Corbino 2 at $B = 9$ T. The red numbers are the filling factors assigned to the conductance dips in the n axis. Blue arrows in (a) and (c) indicate the diagonal conductivity dip line originated from the inactive region of the sample not covered by the top gate. (e) A plot of σ vs the perpendicular magnetic field B and D for Corbino 2 at $n = 0$ and $T = 2.3$ K. The orange broken line indicates the phase boundaries between the canted antiferromagnetic (CAF) and the layer polarized (LP) regions.

a previous study [15]. Here, we convert D^* into the energy unit Δ_{D^*} using the linear relationship between the displacement field and the energy gap at a zero magnetic field:

$$\Delta_{D^*} \equiv \Delta(D^*) \cong 130 \times D^* (\text{V/nm}) (\text{meV}). \quad (1)$$

The function $\Delta(D) = 130 \text{ meV/D (V/nm)}$ is the energy gap induced by applying the displacement field D at a zero magnetic field [19].

The physical meaning of Δ_{D^*} is the difference in the interaction energy between the CAF and LP states, which is overcome by the polarization energy at $D = D^*$.

B. Temperature dependence

Having confirmed the known gate-dependence property of the $\nu = 0$ quantum Hall state, we studied the temperature dependence of the conductivity at the center of the CAF state ($n = 0$, $D = 0$). Owing to the gate leakage problem of Corbino 2 at high temperatures, a wide range of temperature dependences were measured for the Corbino 1, two-terminal, and Hall bar samples. This measurement for Corbino 1 was not affected by its nonactive region because the center of the CAF state is at $V_{\text{TG}} = 0$ and $V_{\text{BG}} = 0$; therefore, the entire sample was in the CAF state.

Figure 3(a) shows the temperature dependence of conductivity in Corbino 1. It exhibits nonmonotonic behavior

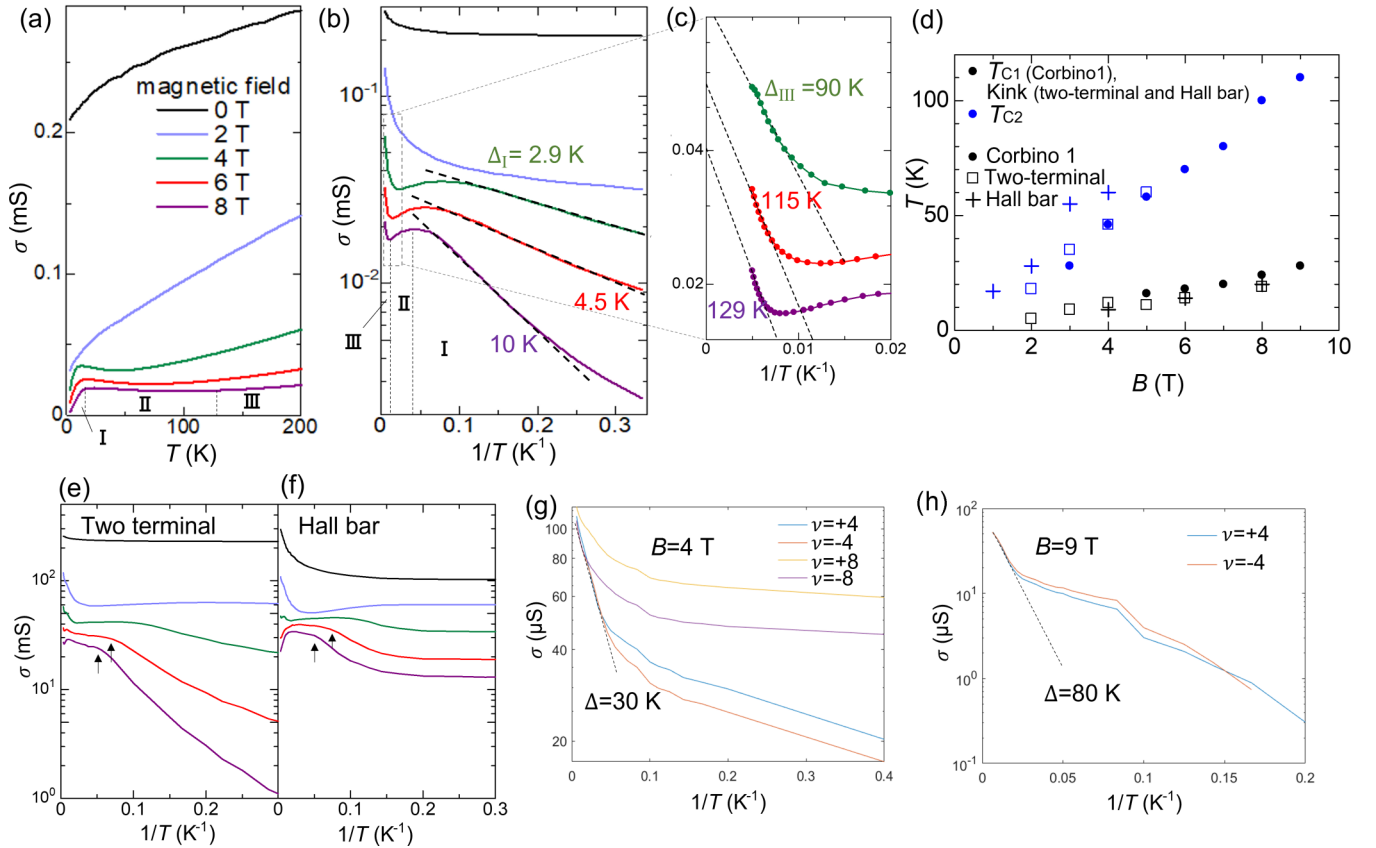


FIG. 3. Temperature dependence of the conductivity and parameters. (a) Standard plot and (b) Arrhenius plot of the temperature dependence of the conductivity for Corbino 1 at $T = 2.3\text{--}200$ K for magnetic fields of 0, 2, 4, 6, and 8 T. The temperature regions separated by black broken lines are regions I, II, and III for $B = 8$ T. (c) Magnified plot of (b) around region III. (d) Magnetic field dependence of T_{C1} of Corbino 1 (black dots), T_{C2} of Corbino 1 (blue dots), the first kink of the two-terminal sample (black open square), T_{C2} of the two-terminal sample (blue open square), the first kink of Hall bar sample (black cross), and T_{C2} of Hall bar sample (blue cross). Temperature dependence of the conductivity of (e) two-terminal and (f) Hall bar samples in Arrhenius plot. Black arrows indicate the first kink, whose magnetic field dependence is shown in (d). Temperature dependence of the conductivity of Corbino 1 at $\nu = \pm 4$ and 8 at (g) $B = 4$ T and (h) $B = 9$ T. Black broken lines indicate the Arrhenius fitting in high-temperature region.

above $B = 4$ T. At $B = 8$ T, it behaves as an insulator below $T = 20$ K, a metal at higher temperatures, and an insulator above $T = 80$ K [Fig. 3(a)]. We define these three temperature regions as I, II, and III, respectively. We define the boundary temperature between I and II (II and III) as T_{C1} (T_{C2}), where conductivity takes a local maximum (minimum), and they are shown in Figs. 3(d) and 4(a).

Figure 3(b) is an Arrhenius plot of Fig. 3(a), and Fig. 3(c) is its magnification at high-temperature region. The temperature dependence in Region I is well fitted with the activation energy Δ_I . Region III is roughly fitted by activation energy Δ_{III} , although we observe a slight deviation around the highest temperature, and we must interpret the fitted Δ_{III} as a lower bound of activation gap rather than actual activation gap. Magnetic field dependence of the activation gap is shown in Fig. 4(a) and will be further discussed in Sec. C.

In the two-terminal sample, T_{C1} defined by the local maximum was not defined well under a high magnetic field >6 T, although kinks were observed [black arrows in Fig. 3(e)], which are comparable with T_{C1} of the Corbino sample and might be remnants of T_{C1} [Fig. 3(d)]. In the Hall bar sample,

the first kinks [black arrows in Fig. 3(f)] are comparable with T_{C1} of the Corbino sample [Fig. 3(d)]. In the Hall bar sample and the two-terminal sample, T_{C2} is not well defined for a high magnetic field >6 T. As the vanishing T_{C2} is only observed under a high magnetic field, they might be due to trivial edge conduction. Another possible reason is the sample-dependent amount of impurity.

The nonmonotonic T dependence has been reported in previous studies [11,15,18]. However, its origin has not yet been determined. In a previous study, it was pointed out that nonmonotonicity can originate from the coexistence of bulk and edge states [18]. However, our results in the Corbino sample revealed that the nonmonotonicity of the CAF state is due to an intrinsic bulk property.

Nonmonotonicity of the temperature dependence of the conductivity was not observed at $\nu = \pm 4$ and ± 8 [Figs. 3(f) and 3(g)], indicating that it is related to the electronic correlation. At $\nu = \pm 4$ and ± 8 , temperature dependence is stronger at high temperature and weaker at low temperature. These two temperature regimes are attributed to thermal activation across the LLs and hopping transport, respectively, which is quantitatively consistent with previous research [47].

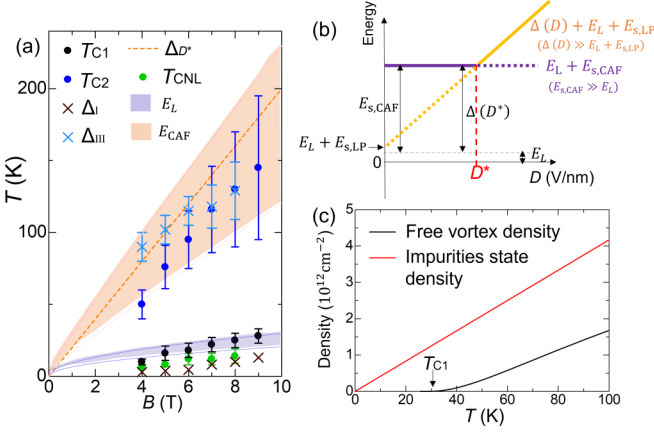


FIG. 4. Parameters and characteristic energy of the temperature dependence and estimation of vortex and impurity densities. (a) Magnetic field dependence of T_{C1} (black dots), T_{C2} (blue dots), Δ_I (black cross), and Δ_{III} (blue cross) in Corbino 1, Δ_{D^*} (orange broken line) in Corbino 2, T_{CNL} (green dots), E_S (blue shade), and E_{CAF} (orange shade). (b) Energy gap (stabilization energy) of the canted antiferromagnetic (CAF) and layer polarized (LP) state as a function of D . The purple (orange) line is the energy gap of the CAF (LP) state as a function of D . Solid lines indicate that it is the ground state. (c) The free vortex density was calculated by $n_{VTX}(T) = A^{-2} \exp(-2B/\sqrt{T/T_{C1} - 1})$, where $A = 0.27 \times$ magnetic length ($= \sqrt{B(= 8 \text{ T})/\Phi_0}$) and $B = 1.99$. The impurity density was calculated by $n_{imp}(T) = 0.043 \times 10^{12} \text{ cm}^{-2} \times T \exp(-2 \text{ K}/T)$.

C. Discussion on the temperature dependence

1. Characteristic energy scale

We now consider the origin of the nonmonotonic T dependence and physical significance of the characteristic temperatures based on the mean-field theory of quantum Hall ferromagnetism. Generally, the energy gap of a quantum Hall ferromagnetic system consists of three terms [25]:

$$E = E_1 + E_L + E_S, \quad (2)$$

$$E_1 = \mu_B B_{\text{total}} + \Delta(D), \quad (3)$$

$$E_L \simeq \frac{e^2}{4\pi\epsilon l_B} \propto \sqrt{B_{\perp}}, \quad (4)$$

$$\begin{aligned} E_S &\simeq \int dr^2 \left[\phi^*(r) \frac{e^2}{4\pi\epsilon a} \phi(r) \right]^2 \\ &= \frac{1}{l_B^2} \int dr'^2 \left[\phi^*(r') \frac{e^2}{4\pi\epsilon a} \phi(r') \right]^2 \quad (r' = r/l_B) \\ &\propto 1/l_B^2 \propto B_{\perp}, \end{aligned} \quad (5)$$

where B_{total} (B_{\perp}) is a total (out-of-plane) magnetic field, ϵ is the in-plane dielectric constant, l_B is the magnetic length, a is the lattice constant, and $\phi(r)$ is the wave function of the zeroth LL.

E_1 represents the one-particle energy, which contains the Zeeman energy and polarization energy. E_L represents Coulomb interaction in a longer scale than a lattice constant that is symmetric in the spin and valley space. Since it does

not depend on lattice-scale spin and valley configuration, it is identical for any spin and valley configuration. This is proportional to the square root of the perpendicular magnetic field. Based on the theoretical calculation, $E_L \simeq 10\sqrt{B[T]} \text{ K}$ is estimated [25].

E_S is the lattice-scale short-range Coulomb interaction, which is valley asymmetric and proportional to the perpendicular magnetic field. This term is different for the different spin and valley configurations.

Here, we consider the energy gap of the CAF state $E_{CAF} = E_{1,CAF} + E_L + E_{S,CAF}$ and that of the LP state $E_{LP} = E_{1,LP} + E_L + E_{S,LP}$ as a function of B and D . When $E_{CAF} > E_{LP}$, the ground state is the CAF state and vice versa.

The CAF state does not have polarization; therefore, $E_{1,CAF}$ is determined only by the Zeeman energy. Since out-of-plane spin canting is $\sim 2^\circ$ under a perpendicular magnetic field, E_1 in the CAF state is $E_{1,CAF} = \sin 2^\circ \mu_B B[T] \text{ K} \simeq 0.025B[T] \text{ K}$.

E_L is identical for any kind of state, and Ref. [25] gives the estimation of $E_L = 10\sqrt{B[T]} \text{ K}$. Regarding E_S , Ref. [25] gives the theoretical estimation for the CAF state $E_{S,CAF} = 10\text{--}20B[T] \text{ K}$. In our experimental range of the magnetic field, $E_{S,CAF} > E_L \gg E_{1,CAF}$, so we can ignore $E_{1,CAF}$.

In the LP state which has the layer polarization, E_1 then becomes $E_{1,LP} = \Delta(D) \simeq 940 \times D(\text{V/nm}) \text{ K}$. Here, $\Delta(D)$ is the polarization energy defined in Eq. (1). E_L is much smaller than $E_{1,LP}$ when the LP state is the ground state because $E_{1,LP} > E_{S,CAF} \gg E_L$.

It is difficult to estimate the value of $E_{S,LP}$. In a previous study, the energy gap of the LP state at $D = 0.2 \text{ V/nm}$ measured by scanning tunneling microscopy is almost independent of the perpendicular magnetic field [48]. This implies that the magnetic-field-dependent term $E_L + E_{S,LP}$ is much smaller than the total energy gap; that is, the total energy gap is mainly determined by $E_{1,LP}$.

Figure 4(b) is a schematic diagram of E_{CAF} and E_{LP} as a function of D . We note that the difference between them at $D = 0$ is given by $\Delta(D^*) = E_{S,CAF} + E_{S,LP} \simeq E_{S,CAF}$.

In Fig. 4(a), we compare the theoretically expected values of $E_{CAF} \simeq E_{S,CAF} + E_L$ and E_L and energy scales in the observed nonmonotonic temperature dependence. As we discussed above, $\Delta(D^*) = E_{S,CAF} + E_{S,LP} \simeq E_{S,CAF} = E_{CAF} - E_L$ is comparable with E_{CAF} given that $E_{S,CAF} \gg E_L$. Also, we find that T_{C1} is comparable with E_L , and T_{C2} and Δ_{III} are comparable with E_{CAF} . This indicates that T_{C1} corresponds to the long-range Coulomb interaction and T_{C2} corresponds to the total energy gap of the CAF state, which is mainly determined by the short-range Coulomb interaction. Therefore, the change of the temperature dependence at T_{C1} is associated with the breaking of the quasi-long-range order (QLRO), and the change at T_{C2} is associated with the breaking of the short-range order or an excitation across the CAF energy gap.

2. Origins of nonmonotonic temperature dependence

We consider the origin of the nonmonotonic temperature dependence of the conductivity based on the correspondence between T_{C1} (T_{C2}) and long (short)-range Coulomb interaction energy. In Region III, the temperature dependence of the conductivity is roughly fitted to the Arrhenius formula [Figs. 3(b) and 3(c)], and its activation energy is comparable with T_{C2} . Therefore, the conduction mechanism should be

thermal excitation across the energy gap of the CAF state, which is mainly determined by the energy scale needed to break the local antiferromagnetic order ($E_{S,CAF}$).

In Region I, the temperature dependence is fitted to the Arrhenius formula with activation energy smaller than T_{C1} , although it slightly deviates and exhibits weaker temperature dependence for <5 K. Because the temperature of Region I is significantly lower than the energy gap, the hopping of carriers excited from the impurity states should be dominant.

In Region II, the temperature dependence becomes metallic. As T_{C1} corresponds to the long-range Coulomb interaction, breaking of the QLRO is expected above T_{C1} . Because the CAF state has in-plane rotational symmetry, this order breaking is represented by the KT transition associated with the creation of unbounded vortices and antivortices. The creation of vortices and antivortices can affect the conductivity in the following two ways. First, these vortices can act as scattering centers of the electron spin-flipping process for independently excited free electrons. This increases the scattering rate of the electron and contributes to the decrease in conductivity.

Second, on the other hand, vortices in quantum Hall states have electrical charges and can act as conductive carriers, which contribute to the increase of conductivity.

Whether the conductivity decreases or increases above T_{C1} depends on which are dominant carriers, individually excited free electrons, or collectively excited vortices.

In the next section, we estimate the number of vortices and impurities. The result of the estimation indicates that the number of individually excited electrons and holes from impurity states is much larger than the number of vortices near the KT transition temperature. In such a situation where the conduction is not dominated by vortices but by individually excited carriers, the number of conductive carriers does not change significantly at the KT transition. Therefore, the creation of unbounded vortices results in a decrease in conductivity because increased vortices promote spin flips of electrons and holes, which increases the number of possible scattering processes. As the temperature increases, more vortices are created, and the scattering rate is increased. This type of conductivity reduction is generally observed in the ordered-disordered magnetic phase transition of most magnetic materials. A well-known example is a butterfly-shaped magnetoresistance at the magnetization flip of Ising ferromagnets due to increased domain wall owing to the magnetization flip [49]. It is also known that the creation of skyrmions enhances the magnetic scattering and leads to increased resistance compared with the ferromagnetic phase [50].

3. Vortices density above KT transition

As discussed in the previous sections, T_{C1} is thought to be assigned to the KT transition temperature T_{KT} . Above T_{KT} , free vortices and antivortices that have electrical charges are excited. Here, we estimate the free vortex density and argue that it makes a small contribution to the number of conduction carriers.

The density n_{VTX} of the vortices and antivortices is proportional to $1/\xi_{KT}^2$ [44], where ξ_{KT} is the correlation length (the typical distance between vortices and antivortices). According

to the KT theory [54], the temperature dependence of ξ_{KT} above the KT transition is

$$\xi_{KT} = A \exp\left(\frac{B}{\sqrt{T/T_{KT} - 1}}\right), \quad (6)$$

where A is a length-dimension constant, and B is a dimensionless constant with an order of unity. Because the conductivity dominated by vortices should be proportional to n_{VTX} [44], the temperature dependence of the conductivity arising from free vortex motion is

$$\sigma_{VTX} \propto A^{-2} \exp\left(-\frac{2B}{\sqrt{T/T_{KT} - 1}}\right). \quad (7)$$

If the free vortices are the main conduction mechanism around T_{C1} , the conductivity should exponentially increase above T_{C1} according to Eq. (7). However, we observe a decrease in conductivity above T_{C1} . This indicates that free vortices are not the main conduction mechanism at approximately T_{C1} . To test this hypothesis, we estimated the free vortex density and compared it with another possible conduction mechanism: carriers excited from charged impurities.

The proportional coefficient A of Eq. (6) is $\sim 0.27 \times$ the lattice constant (magnetic length) according to the theoretical calculation [55]. In the same theoretical calculation, $B = 1.99$ is reported. Using these values, we calculated the free vortex density $1/\xi_{KT}^2$ assuming $T_{C1} = T_{KT}$ and plotted it [Fig. 4(c)]. The impurity density was calculated based on the theoretical calculation [30] from the correspondence between the impurity density and the magnetic field at which the CAF state begins to be observed. We observed the CAF state as a conductivity gap above $B = 4$ T in Corbino 1 at $T = 2.3$ K. This corresponds to the density of the impurity states of 0.1×10^{12} cm $^{-2}$ in the energy window of 2.3 K. Here, we assume that the density of the impurity states is constant to the energy [56]; $D_{imp}(T) = C$. The density of the impurity states involved in the scattering process at temperature T is $n_{imp}(T) = C \int_{\Delta}^{\infty} \exp(-\varepsilon/T) d\varepsilon = TC \exp(-\Delta/T)$, where Δ is the average energy spacing between the impurity states. By fitting the temperature dependence of the conductivity below T_{C1} to this function, we obtained $\Delta = 2$ K. Using the relation $C \times 2.3 = 0.1 \times 10^{12}$ cm $^{-2}$, we plotted the $n_{imp}(T)$ [Fig. 4(c)]. Because the density of the nonimpurity states is zero in the CAF energy gap, $n_{imp}(T)$ is the total density of states of the conductive carrier below T_{C1} . Above T_{C1} , the free vortex can be an additional conduction carrier.

Because $n_{imp}(T)$ is much larger than the free vortex density in the vicinity of T_{C1} , the KT transition does not lead to a significant increase in the total conductive carriers above T_{C1} , which could explain why we observe a reduction in conductivity above T_{C1} rather than an increase in conductivity due to the additional carriers of the free vortices.

In addition, we discuss the discrepancy of the KT transition temperatures between this paper and a previous study in monolayer graphene [11]. In Ref. [11], they measured magnetic field dependence of the conductivity at 0.3 K and interpreted it as a magnetic-field-induced KT transition. In their analysis, 0.3 K is above the KT transition temperature at the magnetic field <18 T. This estimation of the KT transition

temperature is much lower than T_{C1} in this paper. A possible reason for this discrepancy is the difference in mobility of the samples. According to theory [44], the KT transition temperature strongly depends on the density of impurities, i.e., mobility. Considering >7 times larger mobility in our samples than that of their samples [11], the discrepancy of the KT transition temperature is consistent with the theoretical calculation [44].

D. Nonlocal transport measurement

Finally, we employ nonlocal transport measurement to get further insight into this scenario. The CAF state can be described by the LL splitting between different spin and valley degrees of freedom, as shown in Fig. 5(a). In this state, Hall conductivity is both spin and valley contrasting. Spin-valley Hall conductivity defined by $\sigma_{SVH} = \sigma_{H, \rightarrow K} - \sigma_{H, \rightarrow K'} - \sigma_{H, \leftarrow K} + \sigma_{H, \leftarrow K'}$ is expected to be nonzero. Here, $\sigma_{H, ij}$ denotes the Hall conductivity for the electron with right or left spin ($i = \rightarrow, \leftarrow$) and K or K' valley ($j = K, K'$), where the right and left spins are in-plane and determined by spontaneous symmetry breaking of in-plane spin rotational symmetry.

Here, σ_{SVH} allows for the conversion between the charge current and spin-valley current, where the spin-valley current is defined by $j_{SV} = j_{\uparrow K} - j_{\uparrow K'} - j_{\downarrow K} + j_{\downarrow K'}$. Assuming that σ_{SVH} is homogeneous over the entire sample, we can expect nonlocal resistance in the Hall bar geometry which originates from the spin-valley current generation and detection, in analogy with spin Hall effect and valley Hall effect.

In the actual sample, σ_{SVH} cannot be homogeneous because the CAF state has continuous spin rotational symmetry, and long-range order does not exist according to Mermin-Wagner theorem. However, if the correlation length of the QLRO in the CAF state is comparable or longer than the sample dimension, integration of σ_{SVH} in the entire sample is not averaged out, and we can expect the spin-valley Hall effect. In the case that the correlation length is smaller than the sample, σ_{SVH} is averaged out and spin-valley Hall effect is not expected [Fig. 5(d)]. That is why the spin-valley Hall effect is the signature of QLRO in the CAF state.

In our previous study [43], we measured the nonlocal resistance in the Hall bar sample and revealed its origin. The nonlocal resistance is defined by V_{3-5}/I_{2-6} with the geometry of terminals shown in Fig. 5(b). By measuring the temperature and magnetic field dependence, we concluded that the main origin of the nonlocal resistance in the CAF state is the spin-valley Hall effect. In this paper, we used the same Hall bar sample [Fig. 5(b)] and measured the nonlocal resistance in a wider temperature range. Since this sample has a comparable size with the Corbino sample, it is reasonable to compare the degree of QLRO in these two samples.

Here, we measured the T dependence of the nonlocal resistance in the range of 1.5 to 50 K. We previously found that nonlocal resistance has a cubic scaling relationship with the local resistance at low temperatures, which is consistent with the model that assumes homogeneous spin- and valley-dependent Hall conductivity in the entire sample [43]. In Fig. 5(c), we show R_{NL}/R_L^3 as a function of temperature.

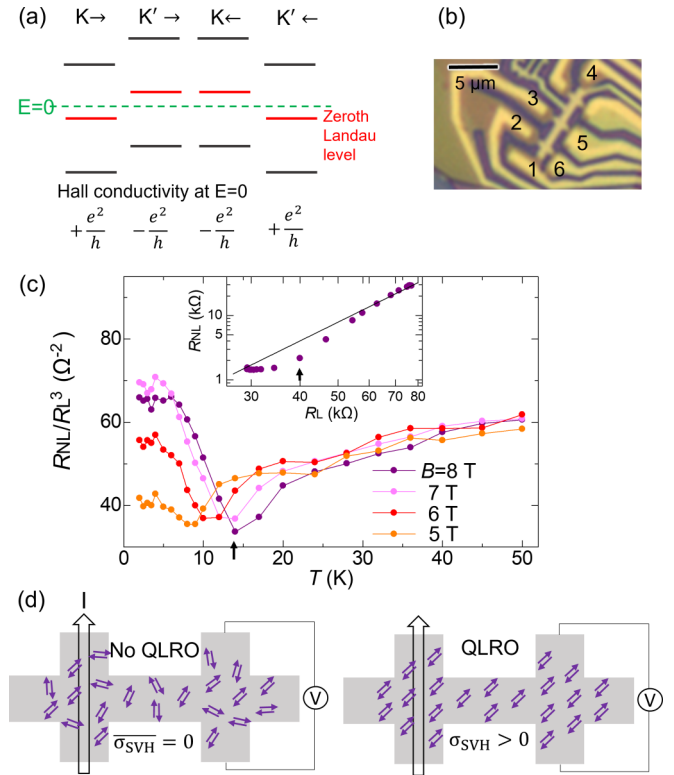


FIG. 5. Nonlocal transport measurement. (a) Schematic of the Landau level (LL) splitting and spin and valley contrasting Hall conductivity. Vertical direction indicates the energy. The gray lines are the energy level of LLs for different spins (\rightarrow, \leftarrow) and valleys (K, K'). A Green broken line indicates zero energy. (b) Optical microscope image of the Hall bar sample and terminal numbers. The nonlocal resistance is defined by V_{3-5}/I_{2-6} . (c) The plot of R_{NL}/R_L^3 as a function of temperature in the Hall bar sample. The arrows indicate T_{CNL} . T_{CNL} for $B = 8$ T. The inset shows R_{NL} as a function of R_L at $B = 8$ T in the same temperature range. The black line and arrow indicate cubic dependence and T_{CNL} , respectively. (d) Schematic of the phase transition and spin-valley Hall conductivity in the canted antiferromagnetic (CAF) state. At low temperatures ($T < E_L$, bottom), vortices and antivortices are always bound, and the system has a quasi-long-range order (QLRO). In this case, the average of the spin-valley Hall conductivity over the sample is nonzero. Above $T = E_L$, QLRO is broken, and the correlation length begins to exponentially decrease as the temperature increases, but antiferromagnetic orders are still preserved locally (top). In this case, the average of the spin-valley Hall conductivity over the sample is zero.

It is nearly constant at low temperatures, indicating the homogeneous spin- and valley-dependent Hall conductivity. At higher temperatures, it drops and exhibits a dip [a black arrow in Fig. 5(c)]. This drop indicates a drop in the spin- and valley-dependent Hall conductivity or collapse of its homogeneity. At higher temperatures, it increases as the temperature increases, indicating another mechanism of nonlocal transport, such as the thermal effect [43,57].

We defined the dip temperature as T_{CNL} and plotted it in Fig. 4(a). Here, T_{CNL} increases as B increases and is comparable with E_L and T_{C1} . This supports the scenario that KT transition occurs, and QLRO is broken at T_{C1} .

IV. CONCLUSIONS

In summary, we observed nonmonotonic temperature dependence of the conductivity in the CAF state characterized by two different energy scales. Based on the mean-field theory of quantum Hall ferromagnetism, we attribute these to the KT transition and the breaking of the local antiferromagnetic order. This is the first observation of a two-step temperature-induced phase transition of a quantum Hall magnet, which was theoretically argued for the $\nu = 0$ quantum Hall state of monolayer graphene [44]. In Mott insulators, a similar two-step phase transition associated with the breaking of the long- and short-range antiferromagnetic orders is commonly observed [51–53], indicating the similarity between quantum Hall systems and correlated crystals. This paper could inform further studies of temperature-induced phase transitions in quantum Hall magnetic systems as gate-controllable experimental platforms.

ACKNOWLEDGMENTS

M.Y. and S.T. acknowledge support from KAKENHI (Grants No. 26220710, No. 17H01138, and No. JP19H05610). K.W. and T.T. acknowledge support from the Elemental Strategy Initiative conducted by the MEXT, Japan (Grant No. JPMXP0112101001) and JSPS KAKENHI (Grants No. JP19H05790 and No. JP20H00354). K.N. acknowledges support from JSPS KAKENHI (Grant No. JP20H01830) and CREST (Grant No. JPMJCR18T2).

APPENDIX A: FABRICATION DETAIL

We used a mechanical exfoliation technique to prepare BLG and h-BN flakes. The number of layers in each graphene flake on the SiO_2 (285 nm)/Si substrate was determined by the contrast of the optical microscope image. After choosing clean h-BN and graphene flakes using AFM, we stacked them. First, an h-BN flake was picked up using a stamp made of a polycarbonate thin film on a round polydimethylsiloxane (PDMS). The thickness of an h-BN flake is roughly estimated to be 30–50 nm from its color in an optical microscope image. We then picked up a BLG flake with the h-BN flake and released them on another h-BN flake with a thickness of ~ 30 –50 nm for the Corbino 1 and two-terminal samples. For the Corbino 2 and Hall bar samples, we picked up the second h-BN flake and released the h-BN/BLG/h-BN stack on the graphite, whose thickness was ~ 5 –10 nm. Graphite

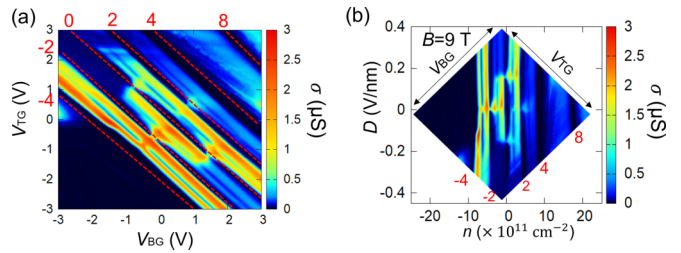


FIG. 7. Dual gate dependence of the conductivity in Corbino 2 measured at $B = 9$ T and $T = 2.3$ K. (a) Conductivity vs the top gate voltage V_{TG} and back gate voltage V_{BG} . The red numbers indicate the filling factors for conductivity dips indicated by broken red lines. (b) Conductivity vs the carrier density n and displacement field D . This figure is identical to Fig. 2(d).

was used as a back gate for these two samples. After they were fabricated, the h-BN/BLG/h-BN/(graphite) stacks were annealed at 380 °C in an Ar/H₂ atmosphere for 1.5 h to remove the polycarbonate residue.

The top gate (Pd 5 nm/Au 30 nm) and Ohmic contacts (Pd 20 nm/Au 100 nm) were defined by electron beam lithography and metal deposition by thermal evaporators [Fig. 6(a)]. Then for the two Corbino samples, another h-BN (20–40 nm thickness) was placed on the top gate as an insulating layer between the outer Ohmic contact and electrodes for the center Ohmic contact and the top gate. We created holes on the h-BN by reactive ion etching in an Ar/O₂/CF₄ atmosphere [Fig. 6(b)], and electrical contact was made to the top gate and center Ohmic contact (Ti 5 nm/Au 250 nm) [Fig. 6(c)].

APPENDIX B: DUAL GATE DEPENDENCE AND CONVERSION TO THE n AND D PLOT

In Fig. 7(a), we show the dual-gate dependence of the conductivity measured at $B = 6$ and 9 T with $T = 2.3$ K. The gate voltages were converted into the carrier density and displacement field as follows:

$$n = \frac{\epsilon_{\text{TG}}}{ed_{\text{TG}}} V_{\text{TG}} + \frac{\epsilon_{\text{BG}}}{ed_{\text{BG}}} V_{\text{BG}}, \quad (\text{B1})$$

$$D = -\frac{\epsilon_{\text{TG}}}{d_{\text{TG}}} V_{\text{TG}} + \frac{\epsilon_{\text{BG}}}{d_{\text{BG}}} V_{\text{BG}}. \quad (\text{B2})$$

Here, ϵ_{TG} and ϵ_{BG} are dielectric constants of the insulating layers for the top and back gates, respectively, e is

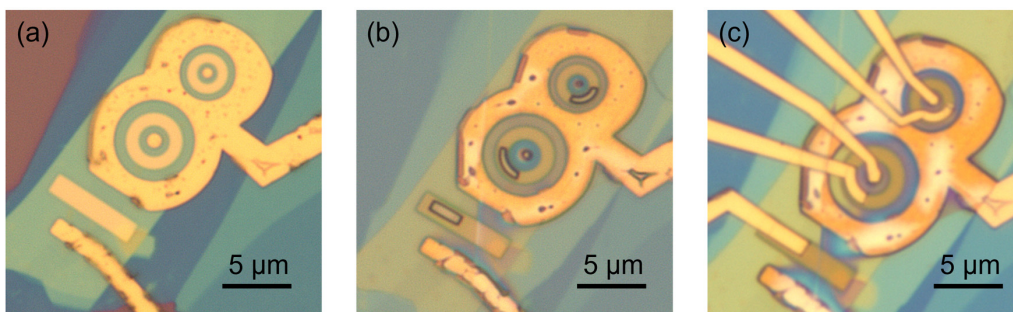


FIG. 6. Sample fabrication processes. Optical microscope images of Corbino 1 (a) after fabricating a top gate and Ohmic contacts, (b) after making holes on the top h-BN by means of reactive ion etching, and (c) after fabricating electrodes for the top gate and Ohmic contacts (completed sample).

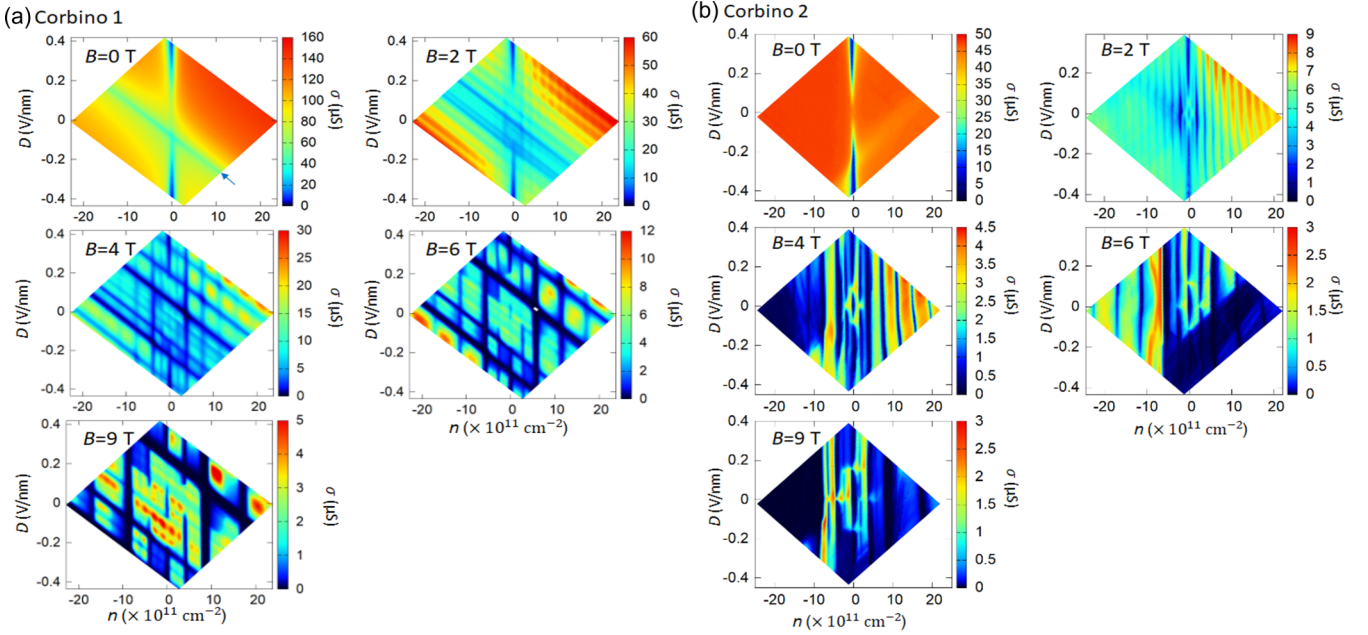


FIG. 8. n and D dependence of the conductivity in (a) Corbino 1 and (b) Corbino 2 measured at $B = 0, 2, 4, 6, 9$ T and $T = 2.3$ K. A blue arrow for Corbino 1 at $B = 0$ T indicates the diagonal conductivity dip line originated from the inactive region of the sample not covered by the top gate.

the elementary charge, d_{TG} and d_{BG} are thicknesses of the insulating layers for the top and back gates, respectively. In our Corbino sample, we adopted $\epsilon_{\text{TG}} \cong 4\epsilon_0$ (h-BN) and $\epsilon_{\text{BG}} \cong 3.58\epsilon_0$ (SiO₂). Here, the difference in the dielectric constants between h-BN and SiO₂ for the back-gate insulating layer was ignored, which resulted in a small uncertainty of D that was less than a few percent.

After the assignment of the filling factor, as shown in Fig. 7(a) and using the expected degeneracy of LLs at $B = 9$ T, we derived the values of the proportional coefficients in Eq. (B1) as

$$\begin{aligned} \frac{\epsilon_{\text{TG}}}{ed_{\text{TG}}} &= 5.8 \times 10^{15} \text{ m}^{-2} \text{ V}^{-1}, \\ \frac{\epsilon_{\text{BG}}}{ed_{\text{BG}}} &= 0.71 \times 10^{15} \text{ m}^{-2} \text{ V}^{-1}. \end{aligned} \quad (\text{B3})$$

These coefficients correspond to the thickness of the top h-BN (38.12 nm) and the total thickness of SiO₂ and bottom h-BN (280 nm), which agree with the expected thicknesses. By substituting these thicknesses into Eq. (B2), we derived the displacement field D and obtained the n and D plots shown in Fig. 7(b).

Next, we show the n and D dependences of the conductivity at $B = 0, 2, 4, 6,$ and 9 T in Corbino 1 and 2. In Corbino 1, diagonal lines appeared in a direction perpendicular to the V_{BG} axis (blue arrow in Fig. 8). These lines corresponded to the minimum conductivity of the inactive region not covered by the top gate. On the other hand, the inactive region in Corbino 2 was highly doped by the Si back gate, and its conductivity was much higher than that of the active region. Therefore, the measured conductivity was mainly determined by the active region, and the diagonal lines were not observed. The conductivity dip at $n = 0$ and $D = 0$ indicates that the

formation of the CAF state appears above $B = 4$ T for Corbino 1 and $B = 2$ T for Corbino 2.

APPENDIX C: TEMPERATURE DEPENDENCE IN THE LP STATE

We measured the temperature dependence of conductivity for various D including the LP phase in one sample, as shown in Fig. 9.

In the D and T plot shown in Fig. 9(a), the domelike highly resistive region of the CAF and LP states are observed. The conductance peaks at $\pm D^*$ (border between the CAF and LP states) become broader as temperature increases but do not change their positions (value of D^*). Figure 9(b) shows the cut of Fig. 9(a) at the LP state (red, orange, light-green, and green solid curves) and the CAF state (black, blue, and purple broken curves). All curves show the saturation of conductance increase ~ 20 K ($1/T \sim 0.05$), but the negative dependence

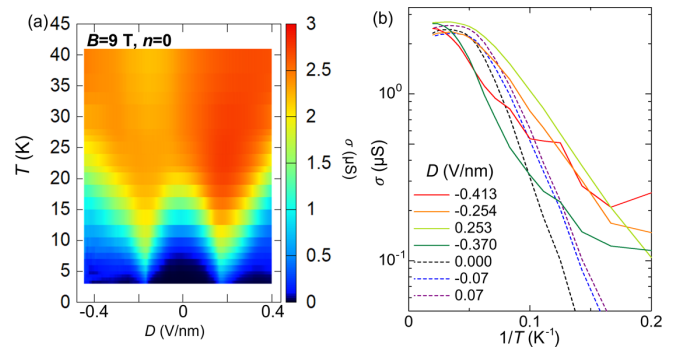


FIG. 9. Temperature dependence of the conductivity for various D at $B = 9$ T in Corbino 2. (a) Color plot of the conductivity as a function of D and T at $n = 0$. (b) Arrhenius plot at different values of D .

of conductance on temperature is only seen in the CAF and LP states at $D = -0.254$ V/nm (close to the CAF). The reduction of conductance is more significant in the CAF state.

In the LP state, the two electrons in each orbital form a spin singlet and occupy the upper or bottom layer. Since they form a spin singlet at a site, it does not have magnetic ordering at least according to the existing theories [25]. Also, layer polarization symmetry in the LP state is externally broken by an out-of-plane electric field; that is, it is not a spontaneous symmetry breaking purely originated from the electron correlation. Even when the temperature exceeds the long-range Coulomb interaction energy, short-range domains are not formed in the LP state due to the external electric field. This is the essential difference between the CAF and LP

states. Therefore, we do not expect a two-step phase transition in the LP state.

Nevertheless, it seems to show saturation of the conductance at a similar temperature with the CAF state. Since the long-range Coulomb interaction energy is identical to the CAF and LP states, there is a possibility that this saturation is related to long-range Coulomb interaction energy.

We could measure only in a limited temperature range (2–42 K) owing to the gate leak problem that started during the measurement. Also, we do not have the data in multiple samples.

To investigate the phase transition in the LP state and the evolution from the CAF state to the LP state, we need more data from multiple samples.

-
- [1] S. M. Girvin and A. H. MacDonald, Multicomponent quantum Hall systems: the sum of their parts and more, in *Perspectives in Quantum Hall Effects: Novel Quantum Liquids in Low-Dimensional Semiconductor Structures*, edited by S. Das Sarma and A. Pinczuk (John Wiley & Sons, Weinheim, 1997), Chap. 5, pp. 161–224.
- [2] S. M. Girvin, The quantum Hall effect: novel excitations and broken symmetries, in *Les Houches Lecture Notes, in Topological Aspects of Low Dimensional Systems*, edited by A. Comtet, T. Jolicœur, S. Ouvry, and F. David (Springer-Verlag, Berlin, Heidelberg, 2000), Vol. 69, pp. 57–175.
- [3] K. Moon, H. Mori, K. Yang, S. M. Girvin, A. H. MacDonald, L. Zheng, D. Yoshioka, and S.-C. Zhang, Spontaneous interlayer coherence in double-layer quantum Hall systems: Charged vortices and Kosterlitz-Thouless phase transitions, *Phys. Rev. B* **51**, 5138 (1995).
- [4] T. S. Lay, Y. W. Suen, H. C. Manoharan, X. Ying, M. B. Santos, and M. Shayegan, Anomalous temperature dependence of the correlated $\nu = 1$ quantum Hall effect in bilayer electron systems, *Phys. Rev. B* **50**, 17725 (1994).
- [5] M. J. Manfra, E. H. Aifer, B. B. Goldberg, D. A. Broido, L. Pfeiffer, and K. West, Temperature dependence of the spin polarization of a quantum Hall ferromagnet, *Phys. Rev. B* **54**, R17327 (1996).
- [6] A. R. Champagne, J. P. Eisenstein, L. N. Pfeiffer, and K. W. West, Evidence for a Finite-Temperature Phase Transition in a Bilayer Quantum Hall System, *Phys. Rev. Lett.* **100**, 096801 (2008).
- [7] Y. Zhao, P. Cadden-Zimansky, Z. Jiang, and P. Kim, Symmetry Breaking in the Zero-Energy Landau Level in Bilayer Graphene, *Phys. Rev. Lett.* **104**, 066801 (2010).
- [8] R. T. Weitz, M. T. Allan, B. E. Feldman, J. Martin, and A. Yacoby, Broken-symmetry states in doubly gated suspended bilayer graphene, *Science* **330**, 812 (2010).
- [9] S. Kim, K. Lee, and E. Tutuc, Spin-Polarized to Valley-Polarized Transition in Graphene Bilayers at $\nu = 0$ in High Magnetic Fields, *Phys. Rev. Lett.* **107**, 016803 (2011).
- [10] A. Veligura, H. J. van Elferen, N. Tombros, J. C. Maan, U. Zeitler, and B. J. van Wees, Transport gap in suspended bilayer graphene at zero magnetic fields, *Phys. Rev. B* **85**, 155412 (2012).
- [11] J. G. Checkelsky, L. Li, and N. P. Ong, Zero-Energy State in Graphene in a High Magnetic Field, *Phys. Rev. Lett.* **100**, 206801 (2008).
- [12] A. J. M. Giesbers, L. A. Ponomarenko, K. S. Novoselov, A. K. Geim, M. I. Katsnelson, J. C. Maan, and U. Zeitler, Gap opening in the zeroth Landau level of graphene, *Phys. Rev. B* **80**, 201403(R) (2009).
- [13] D. A. Abanin, K. S. Novoselov, U. Zeitler, P. A. Lee, A. K. Geim, and L. S. Levitov, Dissipative Quantum Hall Effect in Graphene near the Dirac Point, *Phys. Rev. Lett.* **98**, 196806 (2007).
- [14] B. E. Feldman, J. Martin, and A. Yacoby, Broken-symmetry states and divergent resistance in suspended bilayer graphene, *Nat. Phys.* **5**, 889 (2009).
- [15] P. Maher, C. R. Dean, A. F. Young, T. Taniguchi, K. Watanabe, K. L. Shepard, J. Hone, and P. Kim, Evidence for a spin phase transition at charge neutrality in bilayer graphene, *Nat. Phys.* **9**, 154 (2013).
- [16] A. F. Young, J. D. S. Yamagishi, B. Hunt, S. H. Choi, K. Watanabe, T. Taniuchi, R. C. Ashoori, and P. J. Herrero, Tunable symmetry breaking and helical edge transport in a graphene quantum spin Hall state, *Nature (London)* **505**, 528 (2014).
- [17] S. Pezzini, C. Cobaleda, B. A. Piot, V. Bellani, and E. Diez, Critical point for the canted antiferromagnetic to ferromagnetic phase transition at charge neutrality in bilayer graphene, *Phys. Rev. B* **90**, 121404(R) (2014).
- [18] J. Li, H. Fu, Z. Yin, K. Watanabe, T. Taniguchi, and J. Zhu, Metallic Phase and Temperature Dependence of the $\nu = 0$ Quantum Hall State in Bilayer Graphene, *Phys. Rev. Lett.* **122**, 097701 (2019).
- [19] J. Li, Y. Tupikov, K. Watanabe, T. Taniguchi, and J. Zhu, Effective Landau Level Diagram of Bilayer Graphene, *Phys. Rev. Lett.* **120**, 047701 (2018).
- [20] J. Velasco Jr, L. Jing, W. Bao, Y. Lee, P. Kratz, V. Aji, M. Bockrath, C. N. Lau, C. Varma, R. Stillwell, D. Smirnov, Fan Zhang, J. Jung, and A. H. MacDonald, Transport spectroscopy of symmetry-broken insulating states in bilayer graphene, *Nat. Nanotechnol.* **7**, 156 (2012).
- [21] F. Freitag, J. Trbovic, M. Weiss, and C. Schönberger, Spontaneously Gapped Ground State in Suspended Bilayer Graphene, *Phys. Rev. Lett.* **108**, 076602 (2012).

- [22] Y. Lee, D. Tran, K. Myhro, J. Velasco, C. N. Lau, N. Gillgren, Y. Barlas, J. M. Poumirol, D. Smirnov, and F. Guinea, Competition between spontaneous symmetry breaking and single-particle gaps in trilayer graphene, *Nat. Commun.* **5**, 5656 (2014).
- [23] W. Bao, J. Velasco Jr, F. Zhang, L. Jing, B. Standley, D. Smirnov, M. Bockrath, A. H. MacDonald, and C. N. Lau, Evidence for a spontaneous gapped state in ultraclean bilayer graphene, *Proc. Natl Acad. Sci. USA* **109**, 10802 (2012).
- [24] K. Lee, B. Fallahzad, J. Xue, D. C. Dillen, K. Kim, T. Taniguchi, K. Watanabe, and E. Tutuc, Chemical potential and quantum Hall ferromagnetism in bilayer graphene, *Science* **345**, 58 (2014).
- [25] M. Kharitonov, Canted Antiferromagnetic Phase of the $\nu = 0$ Quantum Hall State in Bilayer Graphene, *Phys. Rev. Lett.* **109**, 046803 (2012).
- [26] M. Kharitonov, Antiferromagnetic state in bilayer graphene, *Phys. Rev. B* **86**, 195435 (2012).
- [27] J. Jung and A. H. MacDonald, Theory of the magnetic-field-induced insulator in neutral graphene sheets, *Phys. Rev. B* **80**, 235417 (2009).
- [28] G. Murthy, E. Shimshoni, and H. A. Fertig, Spin-valley coherent phases of the $\nu = 0$ quantum Hall state in bilayer graphene, *Phys. Rev. B* **96**, 245125 (2017).
- [29] J. Lambert and R. Côté, Quantum Hall ferromagnetic phases in the Landau level $N = 0$ of a graphene bilayer, *Phys. Rev. B* **87**, 115415 (2013).
- [30] K. Nomura and A. H. MacDonald, Quantum Hall Ferromagnetism in Graphene, *Phys. Rev. Lett.* **96**, 256602 (2006).
- [31] J. Alicea and M. P. A. Fisher, Graphene integer quantum Hall effect in the ferromagnetic and paramagnetic regimes, *Phys. Rev. B* **74**, 075422 (2006).
- [32] M. O. Goerbig, R. Moessner, and B. Douçot, Electron interactions in graphene in a strong magnetic field, *Phys. Rev. B* **74**, 161407 (2006).
- [33] E. V. Gorbar, Broken symmetry $\nu = 0$ quantum Hall states in bilayer graphene: Landau level mixing and dynamical screening, *Phys. Rev. B* **85**, 235460 (2012).
- [34] E. V. Castro, N. M. R. Peres, T. Stauber, and N. A. P. Silva, Low-Density Ferromagnetism in Biased Bilayer Graphene, *Phys. Rev. Lett.* **100**, 186803 (2008).
- [35] R. Nandkishore and L. Levitov, Quantum anomalous Hall state in bilayer graphene, *Phys. Rev. B* **82**, 115124 (2010).
- [36] O. Vafek and K. Yang, Many-body instability of Coulomb interacting bilayer graphene: renormalization group approach, *Phys. Rev. B* **81**, 041401 (2010).
- [37] Y. Lemonik, I. L. Aleiner, C. Toke, and V. I. Fal'ko, Spontaneous symmetry breaking and Lifshitz transition in bilayer graphene, *Phys. Rev. B* **82**, 201408 (2010).
- [38] P. Stepanov, S. Che, D. Shcherbakov, J. Yang, R. Chen, K. Thilagar, G. Voigt, M. W. Bockrath, D. Smirnov, K. Watanabe, T. Taniguchi, R. K. Lake, Y. Barlas, A. H. Macdonald, and C. N. Lau, Long-distance spin transport through a graphene quantum Hall antiferromagnet, *Nat. Phys.* **14**, 907 (2018).
- [39] D. S. Wei, T. V. D. Sar, S. H. Lee, K. Watanabe, T. Taniguchi, B. I. Halperin, and A. Yacoby, Electrical generation and detection of spin waves in a quantum Hall ferromagnet, *Science* **362**, 229 (2018).
- [40] S. Takei, A. Yacoby, B. I. Halperin, and Y. Tserkovnyak, Spin Superfluidity in the $\nu = 0$ Quantum Hall State of Graphene, *Phys. Rev. Lett.* **116**, 216801 (2016).
- [41] W. Yuan, Q. Zhu, T. Su, Y. Yao, W. Xing, Y. Chen, Y. Ma, X. Lin, J. Shi, R. Shindou, X. C. Xie, and W. Han, Experimental signatures of spin superfluid ground state in canted antiferromagnet Cr_2O_3 via nonlocal spin transport, *Sci. Adv.* **4**, 1098 (2018).
- [42] F. Zhang, J. Jung, G. A. Fiete, Q. Niu, and A. H. MacDonald, Quantum Hall States in Chirally Stacked Few-Layer Graphene Systems, *Phys. Rev. Lett.* **106**, 156801 (2011).
- [43] M. Tanaka, Y. Shimazaki, I. V. Borzenets, K. Watanabe, T. Taniguchi, S. Tarucha, and M. Yamamoto, Charge Neutral Current Generation in a Spontaneous Quantum Hall Antiferromagnet, *Phys. Rev. Lett.* **126**, 016801 (2021).
- [44] K. Nomura, S. Ryu, and D-H. Lee, Field-Induced Kosterlitz Thouless Transition in the $N = 0$ Landau Level of Graphene, *Phys. Rev. Lett.* **103**, 216801 (2009).
- [45] E. Khalaf, S. Chatterjee, N. Bultinck, M. P. Zaletel, and A. Vishwanath, Charged skyrmions and topological origin of superconductivity in magic-angle graphene, *Sci. Adv.* **7**, 5299 (2021).
- [46] M. J. Zhu, A. V. Kretinin, M. D. Thompson, D. A. Bandurin, S. Hu, G. L. Yu, J. Birkbeck, A. Mishchenko, J. J. V-Marun, K. Watanabe, T. Taniguchi, M. Poloni, J. R. Prance, K. S. Novoselov, A. K. Geim, and M. B. Shalom, Edge current shunt the insulating bulk in gapped graphene, *Nat. Commun.* **8**, 14552 (2017).
- [47] E. V. Kurganova, A. J. M. Giesbers, R. V. Gorbachev, A. K. Geim, K. S. Novoselov, J. C. Maan, and U. Zeitler, Quantum Hall activation gaps in bilayer graphene, *Solid State Commun.* **150**, 2209 (2010).
- [48] L.-J. Yin, L.-J. Shi, L.-Z. Yang, L.-H. Tong, and L. He, Spectroscopic characterization of Landau-level splitting and the intermediate $\nu = 0$ phase in bilayer graphene, *Phys. Rev. B* **101**, 165418 (2020).
- [49] P. Li, L. T. Zhang, W. B. Mi, E. Y. Jiang, and H. L. Bai, Origin of the butterfly-shaped magnetoresistance in reactive sputtered epitaxial Fe_3O_4 films, *J. Appl. Phys.* **106**, 033908 (2009).
- [50] T. Kurumaji, T. Nakajima, M. Hirschberger, A. Kikkawa, Y. Yamasaki, H. Sagayama, H. Nakao, Y. Taguchi, T. Arima, and Y. Tokura, Skyrmion lattice with a giant topological Hall effect in a frustrated triangular-lattice magnet, *Science* **365**, 914 (2019).
- [51] H. Zhao, S. Manna, Z. Porter, X. Chen, A. Uzdeczyk, J. Moodera, Z. Wang, S. D. Wilson, and I. Zeljkovic, Atomic-scale fragmentation and collapse of antiferromagnetic order in a doped Mott insulator, *Nat. Phys.* **15**, 1267 (2019).
- [52] X. Chen, T. Hogan, D. Walkup, W. Zhou, M. Pokharel, M. Yao, W. Tian, T. Z. Ward, Y. Zhao, D. Parshall, C. Opeil, J. W. Lynn, V. Madhavan, and S. D. Wilson, Influence of electron doping on the ground state of $(\text{Sr}_{1-x}\text{La}_x)_2\text{IrO}_4$, *Phys. Rev. B* **92**, 075125 (2015).
- [53] B. Kyung, S. S. Kancharla, D. Senechal, A. M. S. Tremblay, M. Civelli, and G. Kotliar, Pseudogap induced by short-range spin correlations in a doped Mott insulator, *Phys. Rev. B* **73**, 165114 (2006).
- [54] J. M. Kosterlitz, The critical properties of the two-dimensional xy model, *J. Phys. C* **7**, 1046 (1974).

- [55] H. Q. Ding and M. S. Makivic, Kosterlitz-Thouless transition in the two-dimensional quantum XY model, *Phys. Rev. B* **42**, 6827(R) (1990).
- [56] H. Miyazaki, K. Tsukagoshi, A. Kanda, M. Otani, and S. Okada, Influence of disorder on conductance in bilayer graphene under perpendicular electric field, *Nano Lett.* **10**, 3888 (2010).
- [57] J. Renard, M. Studer, and J. Folk, Origins of Nonlocality near the Neutrality point in Graphene, *Phys. Rev. Lett.* **112**, 116601 (2014).